Real-time nanoscale visualization of cholesterol monohydrate nucleation and growth

Lioudmila V. Sorokina [a], Azadeh Amiri [b], Pavel L. Rehak [c], Alireza Ghorbani [b], Abhijit H. Phakatkar [d], Petr Král [e,*], Tolou Shokuhfar [d,*], Reza Shahbazian-Yassar [a,b,**]

[a] *Department of Civil, Materials, and Environmental Engineering, University of Illinois Chicago, Chicago IL 60607, USA*
[b] *Department of Mechanical and Industrial Engineering, University of Illinois Chicago, Chicago IL 60607, USA*
[c] *Department of Chemistry, University of Illinois Chicago, Chicago IL 60607, USA*
[d] *Department of Biomedical Engineering, University of Illinois Chicago, Chicago IL 60607, USA*
[e] *Departments of Chemistry, Physics, Pharmaceutical Sciences, and Chemical Engineering, University of Illinois Chicago, Chicago IL 60607, USA*

ARTICLE INFO

ABSTRACT

Aberrant cholesterol crystallization has implications in the development of numerous pathologies. However, current imaging methods rely on extensive sample preparation and static conditions, unable to capture real-time transformations. This study utilized *in-situ* graphene liquid cell transmission electron microscopy to capture nanoscale events of cholesterol monohydrate (ChM) nucleation and growth. The results revealed ChM triclinic forms through a combination of non-classical and classical modes, specifically, a modified Stranski − Krastanov mechanism. ChM triclinic nucleates from an amorphous precursor, which grows on triclinic surfaces as an epilayer. These epilayers coalesce into 2D layers formed along a preferred lattice plane, enabling 3D growth. Molecular dynamics simulations revealed that the amorphous to crystalline transition occurs via the self-assembly of small clusters, interconnected by filaments, which regrow into bilayers with exposed polar groups. These superstructures adsorb on the surfaces of crystalline cholesterol, form islands, which spread and form nuclei of a new bilayer. This study underscores the significance of homoepitaxy in ChM growth and may provide additional insights into biologically relevant processes, such as ChM nucleation on lipid droplets. Overall, this study lays the foundation for investigating the mechanisms of ChM growth from solution in real-time and on the nanoscale.

1. Introduction

Cholesterol, a major constituent of cellular membranes, has been a focus of numerous studies due to its destructive effects when present in excess [1]. Despite its significance to a variety of biological processes, cholesterol crystallization has long been known to have implications in the development of pathologies such as atherosclerosis and gallstones [2–8]. Additional evidence points to more systemic damage caused by aberrant cholesterol crystallization. For example, cholesterol buildup and subsequent crystallization were identified as contributing to the development of diabetic retinopathy, preventing remyelination in the central nervous system, and influencing renal disease [9–11]. Moreover, it was recently established that cholesterol crystals can cause trauma and promote inflammation in eleven types of cancer in ways similar to those observed in atherosclerosis [12].

Formation of cholesterol monohydrate (ChM) associated with several pathologies was previously reported to occur under supersaturated conditions [6,8]. ChM crystallizes in a stable form as a triclinic structure, which has a plate morphology, and unit cell dimensions of $a = 12.39$ Å, $b = 12.41$ Å, $c = 34.36$ Å, $\alpha = 91.9°$, $\beta = 98.1°$, $\gamma = 100.8°$, with space group P1 [13]. In addition to the triclinic polymorph, anhydrous cholesterol [14], a metastable monoclinic polymorph [15–17] and a monoclinic hemihydrate [18] were previously reported. Recent studies focused on the formation dynamics of ChM triclinic polymorph, observed in atherosclerosis as well as gallstones [19,20]. Moreover, *in vitro* studies demonstrated that the triclinic monohydrate polymorph is associated with cellular plasma membranes [16,21].

Much of the recently gained knowledge related to ChM

crystallization was obtained through time-lapse studies focusing on mechanistic aspects of growth. Of specific interest is the 2D to 3D crystalline growth. Prior work approached this through model membrane and thin film systems, demonstrating that cholesterol segregates into 2D domains which can be used to facilitate 3D crystal growth [15,22–24]. Moreover, it was found that 3D growth occurs through Ostwald ripening, a nonclassical pathway [25,26], and influenced by the epitaxy with the substrate [27–29]. While these results are particularly significant in relation to cell membranes, additional work is needed to better understand transformations of cholesterol in amphiphilic liquid systems related, for example, to cholesterol crystallization inside liposomes.

Presently, there is a dearth of understanding of how ChM triclinic, the most stable polymorph, crystallizes in real time and on the nanoscale. However, advances in imaging techniques make this a possibility. So far, electron microscopy has been used as a characterization tool in enhancing our understanding of cholesterol crystallization processes including those occurring on a cellular level [30–32], analyzing the morphology of crystals obtained from patient samples [33–35], and identifying polymorphism of ChM [16,36]. Yet current characterization methods, such as scanning electron microscopy (SEM) and cryogenic transmission electron microscopy (cryo-TEM), rely on extensive and challenging sample preparations and are unable to capture real-time transformations [37,38].

In the present study, we leveraged the capabilities of *in-situ* graphene liquid-cell (GLC) TEM to observe nanoscale, real-time nucleation and growth of ChM directly from an amphiphilic liquid. The use of *in-situ* GLC TEM was previously reported in studies involving beam-sensitive materials such as biominerals [39–41], bacteria [42,43], proteins [44,45], and ice [46]. Graphene protects the sample from radiation damage while allowing for high spatial resolution and reliable encapsulation [47]. In the current study, we visualized the amorphous to crystalline nanoscale transformation of ChM triclinic and the pathways through which it grows. We observed the homoepitaxial layer-by-layer growth followed by 2D and 3D growth, which can be explained by the Stranski − Krastanov growth model. 3D growth may exhibit subtle misalignments in crystal stacking, likely due to the unique molecular structure of cholesterol. Finally, we revealed how a non-classical pathway is implicated in the ChM triclinic growth. Molecular dynamics (MD) simulations confirmed the non-classical pathway of crystallization via time-dependent self-assembly of cholesterol.

2. Materials and methods

2.1. Experimental

2.1.1. Fabrication of Graphene-Coated TEM grids

Graphene-coated TEM grids for GLC were prepared according to an established protocol [48] and the procedure was previously described in detail [41]. Briefly, commercially CVD-deposited monolayer of graphene-on-copper foil (Grolltex) was used a source of graphene. 200 mesh gold, Quantifoil R2/2 micromachined holey carbon grids (SPI Supplies) were placed on flattened graphene-on-copper foil, with the amorphous carbon side of the grids contacting graphene. Isopropyl alcohol was used to bind graphene and the grids for a minimum of two hours. Once the bonding was complete, copper was etched using a solution composed of 1 g of sodium persulfate (MilliporeSigma) in 10 mL deionized water. After 12 h of copper etching, the graphene-coated grids were rinsed 3 times in HPLC-grade water (MilliporeSigma) followed by air drying.

2.1.2. Sample preparation and encapsulation

100 mg of cholesterol (Avanti Polar Lipids) was dissolved in 80 mL of isopropyl alcohol. As the solution was continuously stirred, 20 mL of water was added and boiled for 30 seconds. The solution was cooled under ambient conditions prior to adding it to the GLC grid. The cholesterol/IPA/water solution was prepared immediately before the encapsulation. To achieve encapsulation, two previously graphene-coated TEM grids were used. 0.3 μL of cholesterol-containing solution was added to the graphene-coated side of the first grid and encapsulated by placing the second grid on top, such that graphene-coated sides of both grids came in contact.

2.1.3. TEM imaging

Imaging was performed using aberration corrected JEOL JEM-ARM200CF microscope operated in TEM mode at 200 kV. A single-tilt TEM holder was used to load GLC following encapsulation. The electron dose was kept constant at 0.015 electrons/Å^2/s. The acquisition of TEM micrographs and videos was performed in real time using Orius CCD camera, capturing 6 frames per second.

2.2. Computational

2.2.1. Molecular dynamics simulations

To closely understand the experimental observations, MD simulations were performed with NAMD3 [49]. Water molecules were described using TIP3P model [50]. Cholesterol parameters were determined in the previous study [51]. Isopropyl alcohol parameter used CHARMM36 general force field [52,53]. The free simulations were performed in the NPT ensemble. Simulations with crystal monolayers were done in the NAPT ensemble, where A was determined by the dimensions of cross section of the monolayer. All simulations were run at a temperature of 298.15 K and pressure of 1 atm using a Langevin dynamics with $\gamma_{Lang} = 1.00$ ps^{-1}. The particle-mesh Ewald (PME) method [54] was used together with periodic boundary conditions for evaluation of long-range Coulomb interactions, where the long-range interactions were evaluated every 1 (van der Waals) and 2 (Coulombic) time steps. The systems were minimized for 5,000 steps and then produced production runs, with a time step set to 2.0 fs.

All solvated systems were constructed using CHARMM GUI [55]. Cholesterol crystal structure was determined through Cambridge Crystallographic Data Center in the previous study [17]. Solvated crystalline systems were constructed as a solvated box placed on the top of a ChM triclinic crystal monolayer. If the solvated box exceeded the dimensions of the crystalline monolayer, there was a pre-equilibration done using NγPT simulations, with γ = -10 dyne/cm without the crystal present. Once the solvent box became smaller, the monolayer cross section, the solvent box was placed upon the crystal monolayer and allowed to pre-equilibrate in NAPT ensemble until the monolayer was solvated. Then production runs were performed. In the simulations involving the crystal monolayer, oxygen atoms and carbons atoms in the rings present in the crystal monolayer were harmonically constrained in both minimization and production runs. In the solvated simulations, O atoms were harmonically constrained in minimization and pre-equilibration, whereas in production runs there were no harmonic constraints. In the crystalline simulations, all solvated cholesterol and non-ring carbon atoms in the crystal were released in the minimization and production runs.

3. Results and discussion

Fig. 1 illustrates the overall experimental approach using *in-situ* GLC TEM methodology and the corresponding representative real-time observation of ChM crystallization pathways. Fig. 1a outlines the steps for GLC preparation and subsequent imaging. Cholesterol was dissolved in isopropyl alcohol with the addition of water to facilitate the formation of ChM. The solution was then confined within two previously graphene-coated TEM grids. This led to the formation of graphene pockets containing the solution, which form due to van der Waals interactions between graphene from the two grids. The inertness of graphene as a substrate has been established, particularly with respect to interactions in binary solutions of water and alcohol [56]. Moreover,
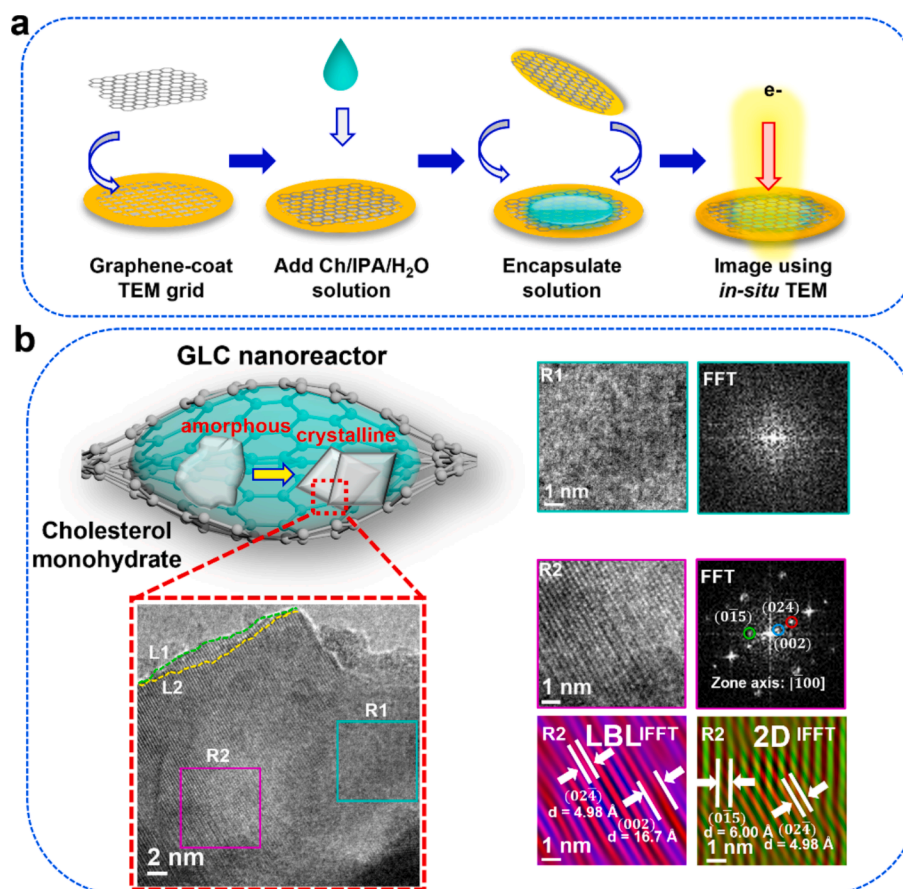
Fig. 1. Experimental approach using *in-situ* GLC method to study real-time cholesterol nucleation and growth. a. Preparation of GLC: TEM grids are coated with graphene, followed by solution encapsulation and imaging. b. A schematic of a GLC with a representative TEM micrograph showing amorphous (teal, R1) and crystalline (pink, R2) regions as well as the formation of layers (green, L1 and yellow, L2), with corresponding FFTs. IFFTs from R2 identify layer-by-layer and 2D growth present.

biomineralization is a temporally and spatially dependent process, and GLC provides a unique environment that effectively mimics these conditions on the nanoscale [40,41]. The liquid layer in GLC maintains solution dynamics comparable to bulk behavior, as its thickness surpasses the critical threshold that could alter fundamental properties [57–60]. The details of the experimental procedures are found in the **Materials and Methods** section.

Then, the solution was exposed to the electron beam, demonstrating the crystallization of ChM from the supersaturated solution, as shown in Fig. 1**b**. It is important to note that electron beam radiation can pose challenges in the TEM imaging of biological materials, including radiolysis, knock-out image, and heating effects, potentially inducing structural degradation [61]. Radiolysis is particularly critical for biological and organic materials, as it causes bond breakage and chemical modifications, potentially influencing nucleation and growth processes. To address these challenges, low-dose imaging was used, with the electron dose was kept constant at 0.015 electrons/$\mathring{A}^2$/s, as previously established [41,62]. Additional best practices to minimize beam damage included minimizing exposure time, beam shielding, and pre-exposure of non-critical areas. These principles guided the experimental design, ensuring that electron beam effects were minimized while maintaining sufficient resolution to capture crystallization phenomena.

A schematic transformation inside a GLC nanoreactor illustrates amorphous and crystalline regions forming in a solution of interest in real time. A corresponding TEM micrograph, shown by a red dotted line, highlights the outcome: layers of cholesterol crystallize (L1 in green and L2 in yellow), with amorphous (teal, R1) and crystalline (pink, R2) regions present. Corresponding fast Fourier transforms (FFTs) confirm the

absence or presence of crystallinity. FFTs and corresponding IFFTs of the crystalline region further confirm the multi-layered nature of the resulting structure in R2 that is visually observed via outlines of L1 and L2 as well as identify two distinct modes of growth present. Layer-by-layer growth is observed, where $(02\bar{4})$ lattice plane with d-spacing of 4.98 Å grows parallel to (002) lattice plane with d-spacing of 16.7 Å. In addition, $(02\bar{4})$ lattice plane forms a single crystal with $(0\bar{1}5)$ lattice plane, d-spacing = 6.00 Å, thus resulting in 2D growth. This example highlights the complexity of ChM mechanisms of growth from a solution observed at the nanoscale.

Stacks of cholesterol crystals of varying size have been previously reported in human and rabbit atherosclerotic lesions [63,64] as well as model and native bile [36]. Moreover, stacking behavior of cholesterol crystals is also observed on cell membranes [63], where they form 2D crystalline domains that develop into assemblies of triclinic crystalline plates [16,24], with multiple crystal accumulation leading to toxicity [65]. However, it is unclear whether there is any particular organizational behavior that governs the formation of these stacks. The following sections further examine the underlying mechanisms behind cholesterol growth and nucleation in real-time.

The events of LBL and 2D growth are further explored in Fig. 2, **Fig. S1** and corresponding **Video S1**. Fig. 2**a** shows time-lapse TEM micrographs, false colored for improved visualization, of events leading to simultaneous LBL and 2D growth in different regions and the subsequent coalescence along a single lattice plane. Corresponding FFTs are presented in Fig. 2**b**. At 4.7 s, the region containing increased contrast and highlighted by a purple box, R1, is amorphous. By 23.7 s, two new regions emerge: R2, false colored in yellow and R3, false colored in pink.
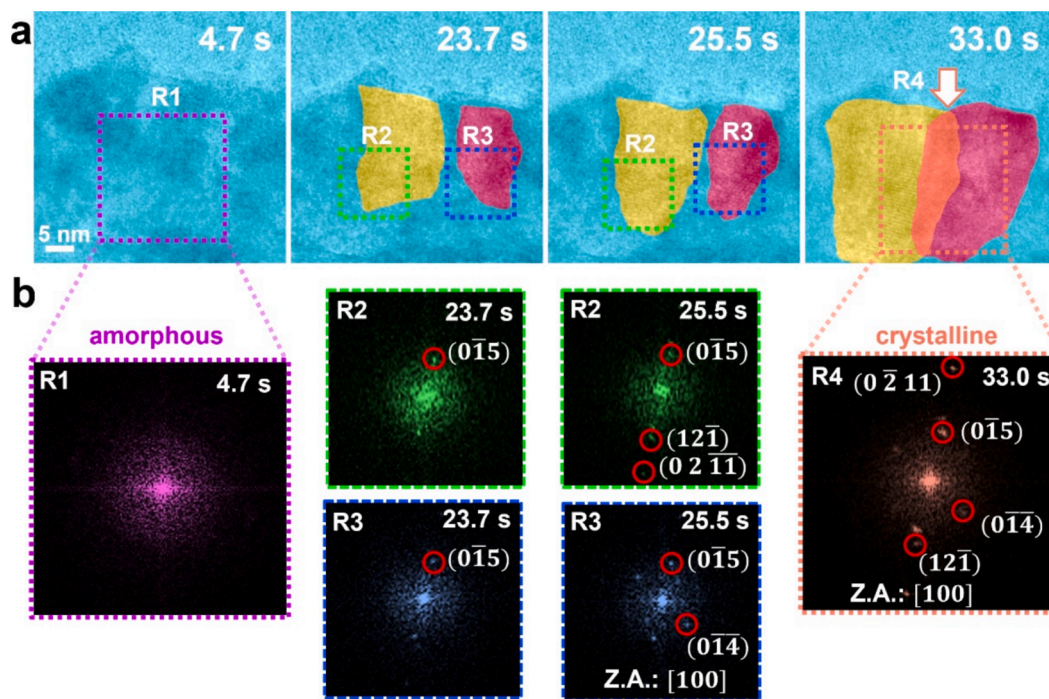
Fig. 2. Visualization of amorphous to crystalline transformation followed by coalescence of ChM. (a) *In-situ* GLC TEM time-lapse micrographs showing nucleation of two crystalline regions, R2 and R3, from a single amorphous region R1. Regions R2 and R3 undergo growth and coalescence to become R4. Scale bar: 5 nm. (b) Corresponding FFTs from select highlighted regions in R1-R4 in (a). For improved visualization, false coloring was used.

Both regions contain $(0\bar{1}5)$ lattice plane, with d-spacing of 6.00 Å. At 25.5 s, parallel to $(0\bar{1}5)$ R2 grows $(02\bar{1}1)$ lattice plane with d = 2.77 Å, and an additional lattice plane $(12\bar{1})$ observed in the same region and appearing parallel to the primary crystal planes, with d = 4.83 Å. This development is indicative of LBL growth. By contrast, at 25.5 s, R3 forms

a triclinic monohydrate crystal, with growth observed in $[0\bar{1}4]$ direction with the [100] zone axis, thus demonstrating 2D growth. At 33.0 s, the two regions undergo growth and coalescence, as highlighted by the overlapping region in orange. The newly formed region, R4, has the characteristics of both R2 and R3; specifically, it exhibits both LBL and 2D growth with the [100] zone axis and an additional lattice plane
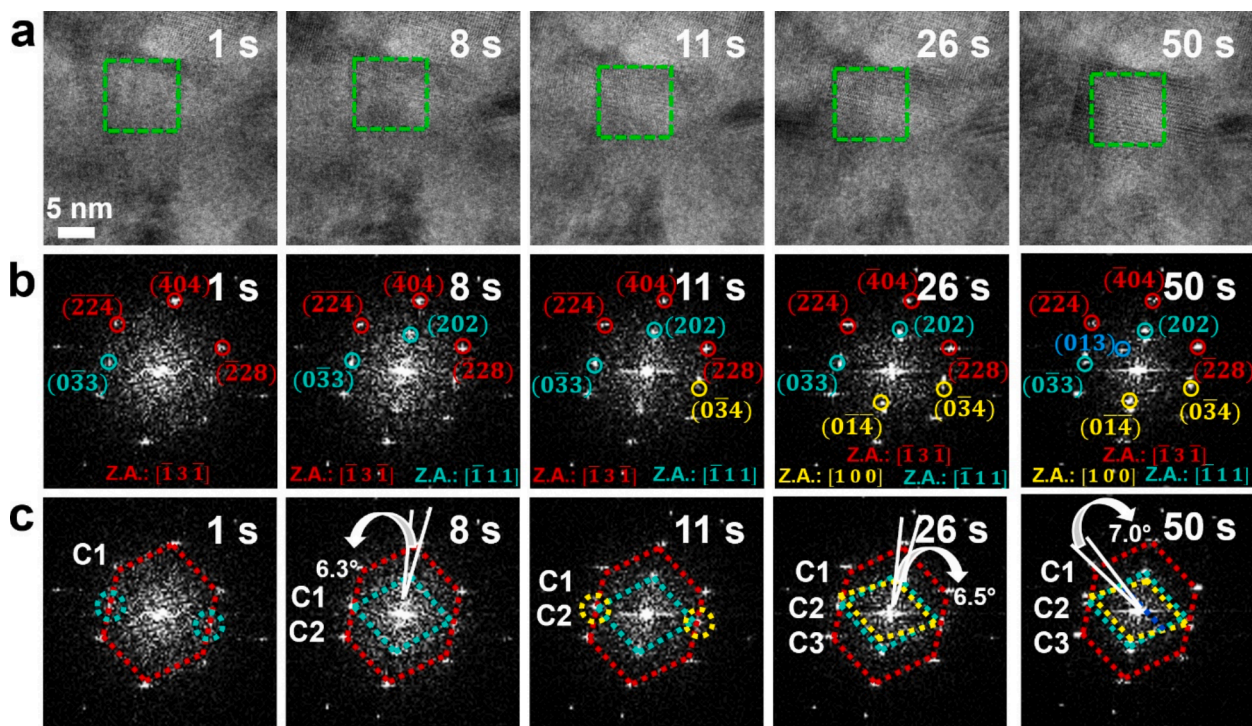
Fig. 3. *In-situ* GLC HRTEM time-lapse (a) micrographs with (b) corresponding FFTs and (c) schematics, illustrating homoepitaxial 3D growth of ChM triclinic. Scale bar: 5 nm.

$(12\bar{1})$.

These events highlight the significance of homoepitaxy to the growth of ChM and act as a starting point for a modified Stranski − Krastanov growth model as a potential mechanism of growth. Stranski − Krastanov growth model can be characterized as a combination of LBL, or Frank-van der Merwe growth followed by Volmer-Weber growth of 3D islands [66]. Stranski − Krastanov growth model was previously used to describe events such as water condensation and ordered growth of amino acid arrays [67,68]. Once the initial layer that is greater in thickness is formed, to release its elastic energy due to a lattice mismatch, 2D − 3D transformation takes place [69,70]. Additional evidence of 3D growth is provided in the following figures.

Fig. 3a and S2 elucidate the epitaxial growth process of a 3D structure on a template crystal through a series of time-resolved TEM micrographs, which were acquired from Video S2. Fig. 3b shows corresponding FFTs while Fig. 3c illustrates the schematic of the time-lapse crystal growth. At 1 s, a single ChM triclinic crystal is observed. This crystal is thereafter referred to as template crystal C1 (red), with corresponding lattice planes $(\bar{2}\,\bar{2}\,\bar{4})$ (d = 3.21 Å), $(\bar{4}04)$ (d = 2.83 Å), and $(\bar{2}28)$ (d = 3.22 Å) and with the zone axis of $[\bar{1}3\bar{1}]$. Also, at this timepoint a single plane, $(0\bar{3}3)$, with d-spacing of 3.84 Å is observed. By 8 s, a new crystal C2 (turquoise) nucleates on the template crystal, including the previously observed, $(0\bar{3}3)$ lattice plane as well as the growth in the [202] direction and zone axis $[\bar{1}11)$. $(0\bar{3}4)$ lattice plane with d = 3.63 Å of a third crystal C3 nucleates by 11 s and by 26 s, growth is visualized in $[0\bar{1}\,\bar{4}]$ direction, with the zone axis of [100]. It is notable that C3 grows with a near-perfect alignment on C2. By 50 s, the growth of (013) lattice plane, marked with blue dotted line with d = 7.72 Å is observed, almost parallel to $(\bar{2}\,\bar{2}\,\bar{4})$ on the original template crystal C1.

In a fundamental work on the crystal structure of cholesterol, Bryan Craven acknowledged the significance of epitaxial growth with another constituent of atherosclerotic plaque, hydroxyapatite, to ChM in biological systems [13]. He postulated that such bonding occurs through the hydrogen bonding of water molecules. Since then, cholesterol epitaxy with biologically-relevant substrates has been studied in phytosterols and phytostanols [71], as well as in calcium phosphate and calcium carbonate systems [29]. For example, ChM was found to form islands on calcite via hydrophilic hydroxyl groups, subsequently undergoing Ostwald's ripening and forming a triclinic platelike morphology [28]. However, despite the significance of epitaxy to cholesterol nucleation and growth, there is a dearth of research from homoepitaxial perspective. Shepelenko *et al.* recently proposed the possibility of ChM nucleation on cholesterol esters [17], which is consistent with our knowledge of cholesterol growth in supersaturated biological environment post-hydrolysis of cholesterol esters. Moreover, a recent report of sheet-like cholesterol crystals representative of late-stage crystallization in human atherosclerotic plaque grown from extracellular lipid droplets [72], further highlighted the need to understand homoepitaxial cholesterol growth mechanism.

The presence of an epitaxial surface leads to the reduction of the nucleation barrier [28]. In the present system, the epitaxy follows the $(\bar{4}04)$ lattice plane on the template crystal C1, as shown in Fig. 3c at 8 s. The resulting (202) lattice plane of C2 forms at a 6.3° angle from the template. Similar rotation is observed at 26 and 50 s as additional planes grow, with 6.5° angle rotation between C2 and C3 and 7.0° rotation between the $(\bar{2}\,\bar{2}\,\bar{4})$ lattice plane of C1 and newly grown (013) lattice plane. Lattice mismatch is characteristic of Stranski − Krastanov growth mode. Lattice strain is relieved when 2D transitions to 3D [70,73]. The limited growth in the *c* direction of any single nanocrystal may be explained by the intercalation of water molecules in hydrophilic region, which prevents the attachment of new molecules [74]. However, this intercalated water layer may serve as a nucleation site for another crystal [13], thus resulting in a 3D growth through multiple layers of crystals. Moreover, while homoepitaxial growth is observed, the alignment between subsequent crystals and the templated crystal is not perfect and is also likely due to the van der Waals interactions in the hydrophilic regions between different crystals. These subtle misalignments between different layers may promote growth as potential nucleation sites for new crystals since they provide additional surface areas for molecules from solution to attach. In general, this growth behavior is representative of the Stranski − Krastanov mode of growth, which results in the epitaxial formation of a 3D growth on a layer associated with the negative surface energy of the substrate and the non-zero lattice misfit [66]. The negative surface free energy of cholesterol originating from the –OH involved in hydrogen bonding [75] coupled with presented experimental data may explain this phenomenon.

Transition from a single layer to multilayer and 3D growth is illustrated in Fig. 4a through a HRTEM micrograph and corresponding FFTs as well as Fig. S3. FFTs for regions 1–3 (R1—R3) were taken to elucidate the epitaxy and transitions between visually observed layers 1–3 (L1-L3). R1 shows the formation of $(0\bar{2}11)$ lattice plane, with d = 2.78 Å and highlighted in red, that acts as a template for epitaxial growth. In R2, an additional $(0\bar{3}2)$ lattice plane, with d = 3.84 Å, forms a crystal with previously observed $(0\bar{2}11)$ lattice plane with [100] zone axis. This growth is highlighted in turquoise. In R3, there is evidence of new layered growth and well as epitaxy-driven 3D growth. Specifically, (014) lattice plane, with d = 6.73 Å, is viewed parallel to $(0\bar{2}11)$ lattice plane. It forms a new crystal with previously observed $(0\bar{3}2)$ lattice plane, with [100] zone axis, highlighted in pink. Similarly, (007) lattice plane, with d = 4.87 Å, is formed parallel to (014) and $(0\bar{2}11)$ lattice planes and creates another crystal with (100) lattice plane, with d = 12.20 Å and with the zone axis along the [010] direction. This crystal is highlighted in yellow. It is important to note the epitaxy that follows both $(0\bar{2}11)$ and $(0\bar{3}2)$ lattice planes and its effect in facilitating nucleation and 3D growth in ChM nanolayers.

To better understand the observed non-classical crystallization of amphiphilic cholesterol, we used molecular dynamics (MD) simulations to model the experimental systems. In the first set of simulations, we wanted to gain insight into the self-assembly of individual solvated cholesterol molecules into clusters and the transition of these semi-amorphous clusters into a crystalline phase. To speed up the self-assembly in the simulations, we have increased the concentrations of cholesterol and made the solvent more polar. Therefore, we have simulated cholesterol at c = 10, 50, and 200 mM concentrations, solvated in 1:1, 1:3, and 4:1 volumetric concentrations (v:v) of IPA:water, respectively. Presumably, all these cholesterol concentrations are oversaturated in the given solvents, which is causing cholesterol condensation.

In Fig. 5, we present the MD-simulated self-assembly of supersaturated cholesterol at different concentrations solvated in different IPA:water (v:v) solvents. As seen in Fig. 5a-c, the cholesterol precipitation is slower in less polar solvents. In the self-assembled clusters, cholesterol molecules tend to have polar heads exposed outside and hydrophobic tails hidden inside; the polar head group is relatively small compared to the adjacent network of rings and alkane tails. In Fig. 5d-e, we present the time-dependent self-assembly of cholesterol at higher concentrations of c ~ 200 mM in 1:1 and 1:3 IPA:water (v:v) solvents, respectively. Again, cholesterol precipitates faster in more polar (1:3) solvent. In these simulations, the superstructures formed start to resemble lipid bilayers, where the polar OH groups are exposed to the solvent and the apolar rings and tail groups coalesce inside the structures. At later times, one can observe extensive finger-like structures formed by the bilayer preassemblies, which could be identified as the gradually changing semi-amorphous phase. These structures are expected to coalesce into larger cholesterol bilayers with protruding OH groups, which would be recognized as crystal nuclei. Eventually, these groups merge, bind with each other, reorganize, and form well defined cholesterol crystals. These simulations reveal the mechanisms of this *non-classical* cholesterol crystallization.
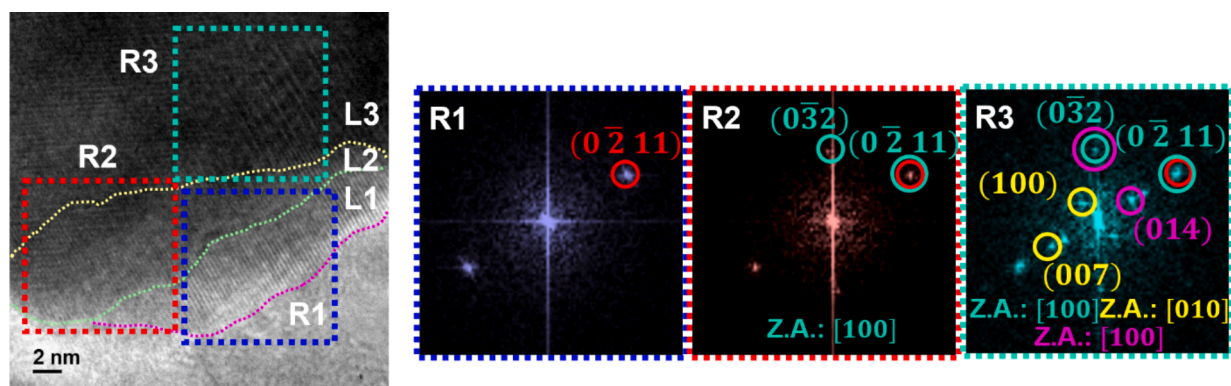
Fig. 4. *In-situ* GLC HRTEM of homoepitaxial growth of ChM. Layered growth L1-L3 is elucidated through corresponding FFTs. R1 serves as a template, followed by crystal growth in R2 and further growth in R3. Scale bar: 2 nm.
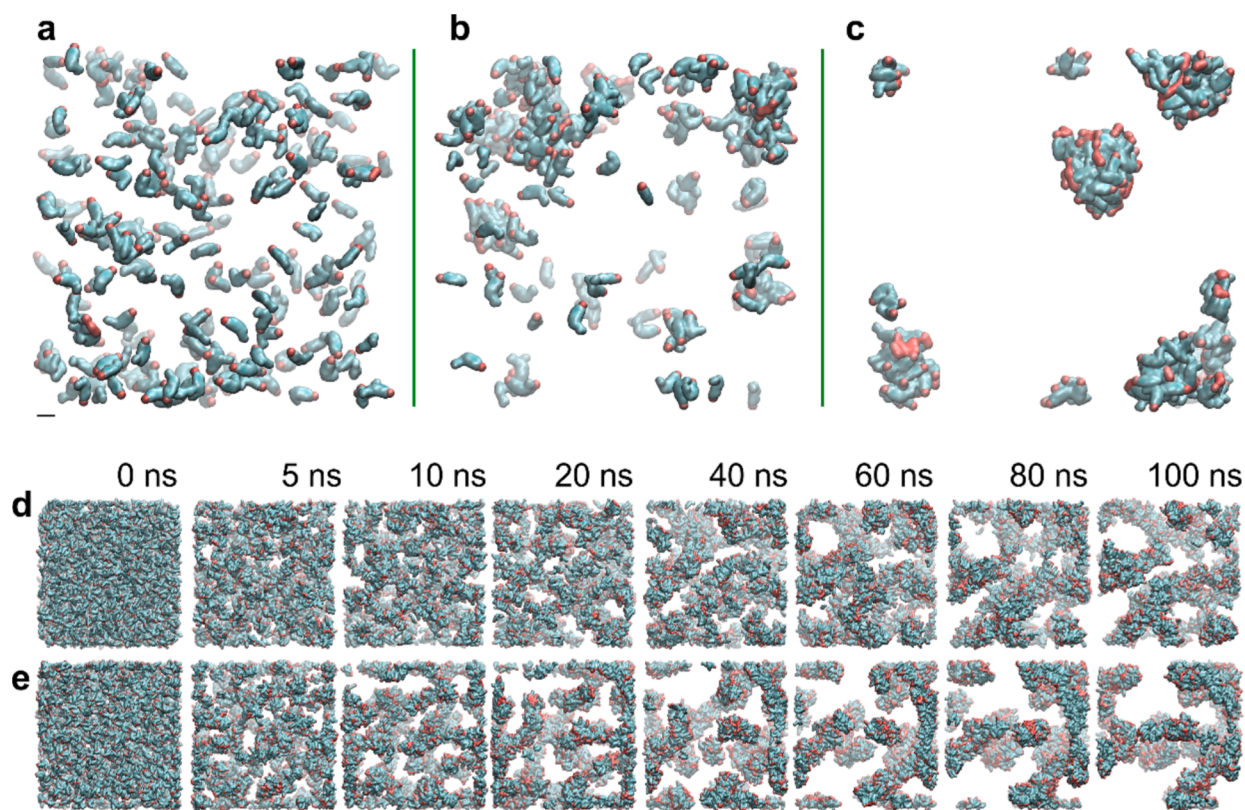

Fig. 5. Cholesterol at 50 mM concentration MD-simulated in IPA:water (v:v) solvent of (a) 4:1 (b), and (c) 1:3, all t = 175 ns. (d-e) 2,000 cholesterol molecules simulated in a cubic box with a side length of l = 25 nm (213 mM) in IPA:water (v:v) solvent of (d) 1:1, (e) 1:3, t = 0, 5, 10, 20, 40, 60, 80 and 100 ns. Red regions correspond to polar OH groups, whereas green regions represent apolar rings and tail groups. Scale bars in captions (a-e) are 1 nm.

Next, we simulated cholesterol (c = 213 mM in 1:1 and 1:3 v:v of IPA: water) in the presence of a triclinic cholesterol crystal; stabilized monolayer of 3,600 cholesterol molecules with polar heads on one side and non-polar tails on the other side [17]. Fig. 6 shows that the solvated cholesterol molecules form clusters that gradually attach on both sides of the crystals in the form of small islands. In the less polar (1:1) solvent (Fig. 6a-d), this attachment appears slower and more reversible than in the more polar (1:3) solvent (Fig. 6e-h). In detail views, we can see that at the top of the crystal (apolar alkyl chains), the cholesterol molecules bind through alkyl-alkyl interactions of the terminal chains, leaving the OH groups exposed to the solvent. In contrast, at the bottom of the crystal (polar OH groups) the cholesterol molecules bind through H-bonding interactions, leaving the alkyl tail group exposed to the solvent. This natural layering would lead to an opportunity for another set of

cholesterol molecules to attach to the layer. The cycle of layers then gradually continues, as proposed in the Stranski − Krastanov growth.

Together with the experimental validation and thermodynamics considerations, MD simulations further support the assignment of the observed crystals as cholesterol monohydrate. The d-spacing values extracted from TEM data exhibit strong agreement with the known crystal structure of cholesterol monohydrate [17]. Furthermore, the experimental conditions in this study closely align with established protocols known to favor cholesterol monohydrate formation [76]. The presence of water in the system, the higher volatility of IPA relative to water, and the impermeability of graphene further corroborate this assignment. Thermodynamically, cholesterol monohydrate is the stable phase in aqueous environments at ambient temperatures, stabilized by a hydrogen bonding network due to water incorporation [16,77]. Finally,
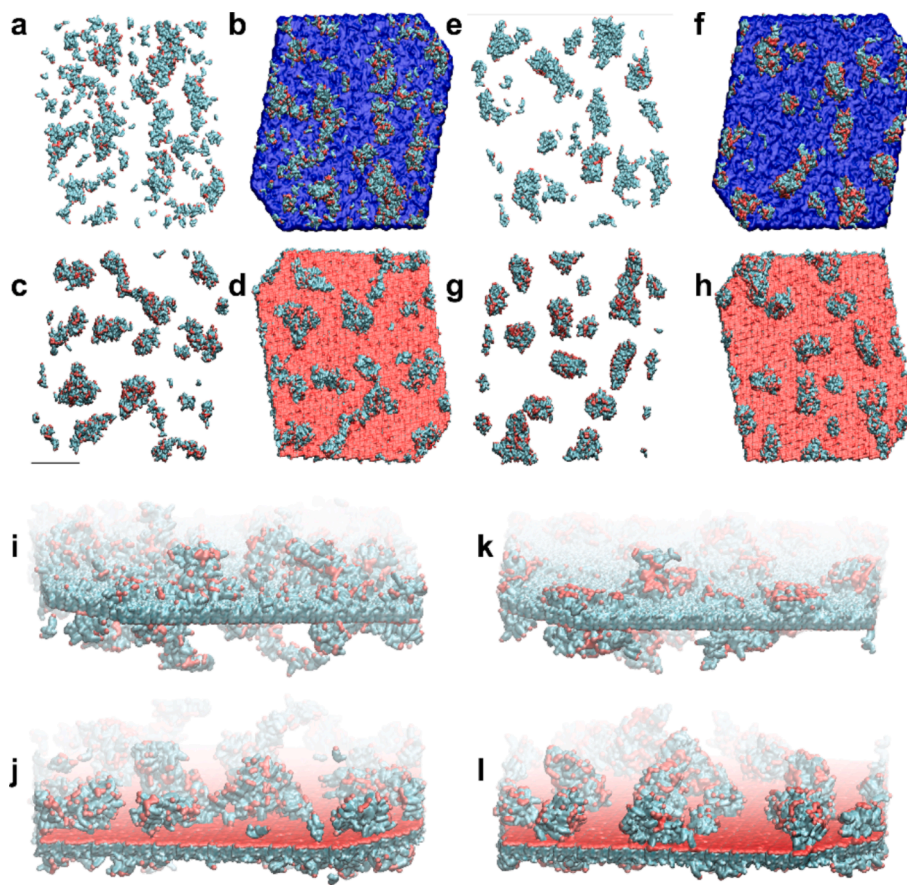
Fig. 6. Simulated systems of cholesterol molecules (213 mM) self-assembling over a triclinic crystal monolayer with 3,600 cholesterol molecules, solvated in IPA: water (v:v) of (a-d, i-j) 1:1 and (e-h,k-l) 1:3 at t = 100 ns. (a,c,e,g) View on the region of clusters that are in contacts with the crystal; (a,e) solvated cholesterol in contact with the crystal alkyl chains; (b,f) view of apolar crystal layer with clusters in contact (c,g) the same for polar the OH head groups; (d,h) view of polar OH groups in contact with clusters; (i,k) view of apolar alkyl layer from an angle; (j,l) view of polar OH-group layer from an angle. Red regions correspond to polar OH groups whereas blue/green regions represent apolar rings and tail groups. Scale bar for captions (a-h) represents 10 nm and scale bar in caption (i-l) represents 1 nm.

MD simulations reinforce this conclusion by demonstrating increased precipitation in more polar solvents, where cholesterol molecules exhibit OH group interactions consistent with the structural organization of cholesterol monohydrate [78].

Based on the evidence presented thus far, Fig. 7 elucidates the proposed mechanism of ChM triclinic growth from a supersaturated solution. First, an epilayer forms from the amorphous precursor in the solution of cholesterol, isopropyl alcohol, and water, followed by homoepitaxial 2D growth. 2D layers undergo coalescence along a preferred lattice plane followed by 3D island growth. The formation of an amorphous precursor phase points to the presence of a non-classical nucleation pathway. Since the solubility of an amorphous phase is greater than that of a crystalline phase at equilibrium conditions, the initial formation of an amorphous phase is in line with Ostwald's rule of stages, which states that a more soluble phase will form first in a supersaturated solution [79].

Interestingly, previous studies, albeit of micron-size crystals [25,26], mention later stage growth events consistent with Ostwald's rule of stages, but to the best of our knowledge, this is the first work to report amorphous to crystalline transformation of ChM at the nanoscale. The formation of the epilayer is likely the result of the ordering of the sterol ring of the cholesterol molecule as the precursor undergoes reorganization [80]. As the 2D layer is grown on the surface of the epilayer with a lattice mismatch, the elastic strain energy increases linearly with the thickness of the 2D layer [70]. The increase in the elastic energy with increase of the thickness of the 2D layer may be relaxed via the formation of dislocations when the critical thickness is reached. In addition, the formation of 3D islands may also lead to elastic stress relaxation due to the free surfaces of the 3D island, a phenomenon observed in the case of ChM triclinic. In addition, the different growth mechanisms are likely to result in different outcomes for the final crystal. For example, in 2D growth, surface energy considerations dominate, leading to smooth,
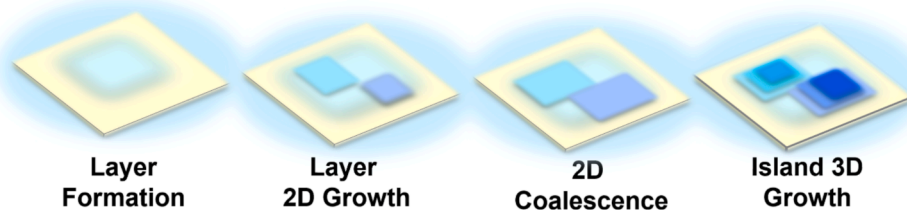
Fig. 7. Schematic representation of the proposed mechanism of ChM triclinic crystal growth.

coherent layers with minimal defects, which enhance stability and uniformity. Conversely, 3D growth is influenced by volumetric energy factors, often resulting in crystals with higher defect densities and structural heterogeneity, potentially reducing stability. The Stranski − Krastanov growth mode, which involves an initial 2D wetting layer followed by 3D island formation due to strain relaxation, combines aspects of both mechanisms, affecting the crystal's morphology and properties and could be further clarified using DFT modeling. Current findings may take us one step closer to unraveling the mystery of ChM growth mechanism on the nanoscale as well as point in the potential areas for targeted dissolution. As the propagation of dislocations in *c* direction was established to be the primary driver for ChM surface dissolution [81], further insights into the surface energy landscape of real-time nanoscale ChM growth may be warranted.

Finally, it is important to note the unique environmental conditions that may contribute to the results described in this work. For example, while previous studies have shown that high pressure exerted within GLCs can stabilize metastable phases [82,83], such as those of calcium carbonate, no metastable phases were observed in this work. Instead, the most stable polymorph, cholesterol monohydrate triclinic, was identified, consistent with its stability under ambient conditions. This suggests that, in this particular system, high-pressure effects do not appear to play a significant role in the crystallization process. In addition, it has been reported that the concentration of the encapsulated solution within the GLC may be higher than that of the native solution due to the drying of the liquid [84]. While this phenomenon remains technically challenging to verify at present, further research could address this to better understand the relationship between the properties of the encapsulated solution and the observed crystallization behavior, providing valuable context and future areas of exploration.

4. Conclusion

Current study visualized real-time nanoscale nucleation and growth of ChM triclinic using *in-situ* GLC TEM. The use of this imaging technique led to an improved understanding of the growth mechanism of ChM triclinic. Specifically, it was established that ChM grows following a modified Stranski − Krastanov mechanism. ChM forms from an amorphous precursor via self-assembly of nanoclusters, first developing an epilayer and then undergoing homoepitaxial 2D layer growth. The 2D layers undergo coalescence along a preferred lattice plane and once the critical thickness is reached, 3D islands form to relax the elastic stress of the layers. This study highlights the significance of homoepitaxy in the growth of ChM and may provide further insights into biologically relevant templated growth, such as plaque on extracellular lipid droplets. Finally, current work paves the way for dynamic materials research approach of ChM on the nanoscale through the *in-situ* GLC TEM methodology.

CRediT authorship contribution statement

Lioudmila V. Sorokina: Writing – original draft, Visualization, Methodology, Investigation, Formal analysis. **Azadeh Amiri:** Writing – review & editing, Methodology, Investigation, Formal analysis. **Pavel L. Rehak:** Writing – original draft, Methodology, Investigation, Formal analysis. **Alireza Ghorbani:** Writing – review & editing, Methodology, Investigation. **Abhijit H. Phakatkar:** Writing – review & editing, Methodology, Investigation. **Petr Král:** Writing – review & editing, Conceptualization. **Tolou Shokuhfar:** Funding acquisition, Conceptualization. **Reza Shahbazian-Yassar:** Writing – review & editing, Supervision, Funding acquisition, Conceptualization.

Declaration of competing interest

The authors declare that they have no known competing financial interests or personal relationships that could have appeared to influence the work reported in this paper.

Appendix A. Supplementary data

Supplementary data to this article can be found online at https://doi.org/10.1016/j.jcrysgro.2025.128096.

Data availability

Data will be made available on request.

References

[1] O.G. Mouritsen, M.J. Zuckermann, *What's so special about cholesterol?* Lipids 39 (11) (2004) 1101–1113.

[2] S. Chakraborty, et al., *How cholesterol stiffens unsaturated lipid membranes*, Proc. Natl. Acad. Sci. 117 (36) (2020) 21896–21905.

[3] G. Szabo, *Dual mechanism for the action of cholesterol on membrane permeability*, Nature 252 (5478) (1974) 47–49.

[4] P. Purdy, M. Fox, J. Graham, *The fluidity of Chinese hamster ovary cell and bull sperm membranes after cholesterol addition*, Cryobiology 51 (1) (2005) 102–112.

[5] T.J. Pucadyil, A. Chattopadhyay, *Role of cholesterol in the function and organization of G-protein coupled receptors*, Prog. Lipid Res. 45 (4) (2006) 295–333.

[6] M.J. Chapman, R.P. Mason, *Cholesterol crystals and atherosclerotic plaque instability: therapeutic potential of eicosapentaenoic acid*, Pharmacol. Ther. (2022) 108237.

[7] M. Whiting, B. Bradley, J. Watts, *Chemical and physical properties of gall stones in South Australia: implications for dissolution treatment*, Gut 24 (1) (1983) 11–15.

[8] H.H. Wang, et al., *Recent advances in the critical role of the sterol efflux transporters ABCG5/G8 in health and disease*, Lipid Transfer in Lipoprotein Metabolism and Cardiovascular Disease (2020) 105–136.

[9] S.S. Hammer, et al., *Cholesterol crystal formation is a unifying pathogenic mechanism in the development of diabetic retinopathy*, Diabetologia (2023) 1–14.

[10] L. Cantuti-Castelvetri, et al., *Defective cholesterol clearance limits remyelination in the aged central nervous system*, Science 359 (6376) (2018) 684–688.

[11] F. Scolari, et al., *Cholesterol crystal embolism: a recognizable cause of renal disease*, Am. J. Kidney Dis. 36 (6) (2000) 1089–1109.

[12] G.S. Abela, et al., *Cholesterol crystals induce mechanical trauma, inflammation, and neo-vascularization in solid cancers as in atherosclerosis*, American Heart Journal Plus: Cardiology Research and Practice (2023) 100317.

[13] B.M. Craven, *Crystal structure of cholesterol monohydrate*, Nature 260 (5553) (1976) 727–729.

[14] H.-S. Shieh, L. Hoard, C.E. Nordman, *Crystal structure of anhydrous cholesterol*, Nature 267 (5608) (1977) 287–289.

[15] I. Solomonov, et al., *Trapping crystal nucleation of cholesterol monohydrate: relevance to pathological crystallization*, Biophys. J. 88 (3) (2005) 1809–1817.

[16] N. Varsano, et al., *Two polymorphic cholesterol monohydrate crystal structures form in macrophage culture models of atherosclerosis*, Proc. Natl. Acad. Sci. 115 (30) (2018) 7662–7669.

[17] M. Shepelenko, et al., *Polymorphism, structure, and nucleation of cholesterol· H2O at aqueous interfaces and in pathological media: revisited from a computational perspective*, J. Am. Chem. Soc. 144 (12) (2022) 5304–5314.

[18] M.B. Al-Handawi, et al., *Mechanical and crystallographic analysis of cholesterol crystals puncturing biological membranes*, Chem.–A European J. 24 (44) (2018) 11493–11497.

[19] H.S. Kruth, *Cholesterol deposition in atherosclerotic lesions*, Cholesterol: Its Functions and Metabolism in Biology and Medicine (1997) 319–362.

[20] P. Portincasa, et al., *Behavior of various cholesterol crystals in bile from patients with gallstones*, Hepatology 23 (4) (1996) 738–748.

[21] N. Varsano, et al., *Development of correlative cryo-soft X-ray tomography and stochastic reconstruction microscopy. a study of cholesterol crystal early formation in cells*, J. Am. Chem. Soc. 138 (45) (2016) 14931–14940.

[22] R. Ziblat, et al., *Structure of cholesterol/lipid ordered domains in monolayers and single hydrated bilayers*, Angew. Chem. Int. Ed. 48 (47) (2009) 8958–8961.

[23] R. Ziblat, et al., *Spontaneous formation of two-dimensional and three-dimensional cholesterol crystals in single hydrated lipid bilayers*, Biophys. J. 103 (2) (2012) 255–264.

[24] N. Varsano, et al., *Formation of 3D cholesterol crystals from 2D nucleation sites in lipid bilayer membranes: implications for atherosclerosis*, J. Am. Chem. Soc. 137 (4) (2015) 1601–1607.

[25] S. Park, et al., *Crystallization of cholesterol in phospholipid membranes follows Ostwald's rule of stages*, J. Am. Chem. Soc. 142 (52) (2020) 21872–21882.

[26] G.J. Ma, et al., *Mechanistic aspects of the evolution of 3D cholesterol crystallites in a supported lipid membrane via a quartz crystal microbalance with dissipation monitoring*, Langmuir 37 (15) (2021) 4562–4570.

[27] D. Hirsch, R. Azoury, S. Sarig, *Co-crystallization of cholesterol and calcium phosphate as related to atherosclerosis*, J. Cryst. Growth 104 (4) (1990) 759–765.

[28] M.C. Frincu, et al., *The epitaxial growth of cholesterol crystals from bile solutions on calcite substrates*, J. Am. Chem. Soc. 126 (25) (2004) 7915–7924.

[29] M.C. Frincu, R.E. Sharpe, J.A. Swift, *Epitaxial relationships between cholesterol crystals and mineral phases: implication for human disease*, Cryst. Growth Des. 4 (2) (2004) 223–226.

[30] Y. Baumer, et al., *Hyperlipidemia-induced cholesterol crystal production by endothelial cells promotes atherogenesis*, Nat. Commun. 8 (1) (2017) 1–14.

[31] C. Marquer, et al., *Increasing membrane cholesterol of neurons in culture recapitulates Alzheimer's disease early phenotypes*, Mol. Neurodegener. 9 (1) (2014) 1–13.

[32] Y. Baumer, et al., Cholesterol crystals and atherosclerosis, Oxford University Press, 2020.

[33] G.S. Abela, *Cholesterol crystals piercing the arterial plaque and intima trigger local and systemic inflammation*, J. Clin. Lipidol. 4 (3) (2010) 156–164.

[34] F. Ghanem, et al., *Cholesterol crystal embolization following plaque rupture: a systemic disease with unusual features*, J. Biomed. Res. 31 (2) (2017) 82.

[35] G.S. Abela, et al., *Effect of cholesterol crystals on plaques and intima in arteries of patients with acute coronary and cerebrovascular syndromes*, Am. J. Cardiol. 103 (7) (2009) 959–968.

[36] D. Weihs, et al., *Biliary cholesterol crystallization characterized by single-crystal cryogenic electron diffraction*, J. Lipid Res. 46 (5) (2005) 942–948.

[37] M. Nasiri, et al., *Role of cholesterol crystals in atherosclerosis is unmasked by altering tissue preparation methods*, Microsc. Res. Tech. 78 (11) (2015) 969–974.

[38] G. Weissenberger, R.J. Henderikx, P.J. Peters, *Understanding the invisible hands of sample preparation for cryo-EM*, Nat. Methods 18 (5) (2021) 463–471.

[39] K. He, et al., *Revealing nanoscale mineralization pathways of hydroxyapatite using in situ liquid cell transmission electron microscopy*, Sci. Adv. 6 (47) (2020) eaaz7524.

[40] D.J. Banner, et al., *In situ liquid-cell TEM observation of multiphase classical and nonclassical nucleation of calcium oxalate*, Adv. Funct. Mater. 31 (18) (2021) 2007736.

[41] L.V. Sorokina, et al., *Nanoscale growth and densification of calcium oxalate crystals*, Cryst. Growth Des. (2023).

[42] A.H. Phakatkar, et al., *Enhanced bacterial growth by polyelemental glycerolate particles*, ACS Appl. Bio Mater. 6 (4) (2023) 1515–1524.

[43] A.H. Phakatkar, et al., *In situ microscopic studies on the interaction of multi-principal element nanoparticles and bacteria*, ACS Nano 17 (6) (2023) 5880–5893.

[44] C. Wang, et al., *High-resolution electron microscopy and spectroscopy of ferritin in biocompatible graphene liquid cells and graphene sandwiches*, Adv. Mater. 26 (21) (2014) 3410–3414.

[45] S. Narayanan, R. Shahbazian-Yassar, T. Shokuhfar, *In situ visualization of ferritin biomineralization via graphene liquid cell-transmission electron microscopy*, ACS Biomater. Sci. Eng. 6 (5) (2020) 3208–3216.

[46] A.H. Phakatkar, et al., *Real-time TEM observations of ice formation in graphene liquid cell*, Nanoscale 15 (15) (2023) 7006–7013.

[47] J. Zhang, et al., *Clean transfer of large graphene single crystals for high-intactness suspended membranes and liquid cells*, Adv. Mater. 29 (26) (2017) 1700639.

[48] M.R. Hauwiller, J.C. Ondry, A.P. Alivisatos, *Using graphene liquid cell transmission electron microscopy to study in situ nanocrystal etching*, JoVE (Journal of Visualized Experiments) 135 (2018) e57665.

[49] J.C. Phillips, et al., *Scalable molecular dynamics with NAMD*, J. Comput. Chem. 26 (16) (2005) 1781–1802.

[50] W.L. Jorgensen, et al., *Comparison of simple potential functions for simulating liquid water*, J. Chem. Phys. 79 (2) (1983) 926–935.

[51] J.B. Lim, B. Rogaski, J.B. Klauda, *Update of the cholesterol force field parameters in CHARMM*, J. Phys. Chem. B 116 (1) (2012) 203–210.

[52] K. Vanommeslaeghe, et al., *CHARMM general force field: a force field for drug-like molecules compatible with the CHARMM all-atom additive biological force fields*, J. Comput. Chem. 31 (4) (2010) 671–690.

[53] W. Yu, et al., *Extension of the CHARMM general force field to sulfonyl-containing compounds and its utility in biomolecular simulations*, J. Comput. Chem. 33 (31) (2012) 2451–2468.

[54] T. Darden, D. York, L. Pedersen, *Particle mesh Ewald: An N· log (N) method for Ewald sums in large systems*, J. Chem. Phys. 98 (12) (1993) 10089–10092.

[55] S. Jo, et al., *CHARMM-GUI: a web-based graphical user interface for CHARMM*, J. Comput. Chem. 29 (11) (2008) 1859–1865.

[56] H.-Y. Huang, et al., *Peculiar wetting behavior of nanodroplets comprising antagonistic alcohol-water mixtures on a graphene surface*, Surf. Interfaces (2024) 104572.

[57] S. Keskin, C. Pawell, N. de Jonge, *Verification of water presence in graphene liquid cells*, Micron 149 (2021) 103109.

[58] J.M. Yuk, et al., *High-resolution EM of colloidal nanocrystal growth using graphene liquid cells*, Science 336 (6077) (2012) 61–64.

[59] S.M. Ghodsi, et al., *In situ study of molecular structure of water and ice entrapped in graphene nanovessels*, ACS Nano 13 (4) (2019) 4677–4685.

[60] M. Textor, N. de Jonge, *Strategies for preparing graphene liquid cells for transmission electron microscopy*, Nano Lett. 18 (6) (2018) 3313–3321.

[61] R. Egerton, *Control of radiation damage in the TEM*, Ultramicroscopy 127 (2013) 100–108.

[62] L.V. Sorokina, et al., *Nickel as a modifier of calcium oxalate: an in situ liquid cell TEM investigation of nucleation and growth*, Nanoscale 16 (8) (2024) 4266–4274.

[63] J. Capua-Shenkar, et al., *Examining atherosclerotic lesions in three dimensions at the nanometer scale with cryo-FIB-SEM*, Proc. Natl. Acad. Sci. 119 (34) (2022) e2205475119.

[64] J. Capua-Shenkar, A. Kaestner, K. Rechav, V. Brumfeld, I. Kaplan-Ashiri, O. Avinoam, C. Speter, M. Halak, H. Kruth, L. Addadi, Cell-mediated cholesterol crystal processing and clearance observed by 3D cryo-imaging in human atherosclerotic plaques, BioRxiv (2023) 2023-11.

[65] R.K. Tangirala, et al., *Formation of cholesterol monohydrate crystals in macrophage-derived foam cells*, J. Lipid Res. 35 (1) (1994) 93–104.

[66] J. Prieto, I. Markov, *Stranski–Krastanov mechanism of growth and the effect of misfit sign on quantum dots nucleation*, Surf. Sci. 664 (2017) 172–184.

[67] J. Song, et al., *Evidence of Stranski–Krastanov growth at the initial stage of atmospheric water condensation*, Nat. Commun. 5 (1) (2014) 4837.

[68] H. Yuan, et al., *Modified Stranski–Krastanov growth of amino acid arrays toward piezoelectric energy harvesting*, ACS Appl. Mater. Interfaces 14 (41) (2022) 46304–46312.

[69] K.A. Lozovoy, et al., *Kinetics of epitaxial formation of nanostructures by Frank–van der Merwe, Volmer–Weber and Stranski–Krastanow growth modes*, Surf. Coat. Technol. 384 (2020) 125289.

[70] V.G. Dubrovskii, Nucleation theory and growth of nanostructures, Springer, 2014.

[71] B. Cantaert, E. Beniash, F.C. Meldrum, *Nanoscale confinement controls the crystallization of calcium phosphate: relevance to bone formation.* chemistry–a, European J. 19 (44) (2013) 14918–14924.

[72] S. Lehti, et al., *Extracellular lipids accumulate in human carotid arteries as distinct three-dimensional structures and have proinflammatory properties*, Am. J. Pathol. 188 (2) (2018) 525–538.

[73] N. Itagaki, et al., *Growth of single crystalline films on lattice-mismatched substrates through 3D to 2D mode transition*, Sci. Rep. 10 (1) (2020) 4669.

[74] N. Varsano, et al., *Crystalline cholesterol: the material and its assembly lines*, Annu. Rev. Mat. Res. 52 (2022) 57–78.

[75] L. Holysz, A. Szczes, E. Chibowski, *Wetting and electrokinetic properties of cholesterol—revisited*, Colloids Surf. A Physicochem. Eng. Asp. 440 (2014) 49–58.

[76] D. Perl-Treves, et al., *Monoclonal antibody recognition of cholesterol monohydrate crystal faces*, Chem. Biol. 3 (7) (1996) 567–577.

[77] C.R. Loomis, G.G. Shipley, D.M. Small, *The phase behavior of hydrated cholesterol*, J. Lipid Res. 20 (4) (1979) 525–535.

[78] R.S. Abendan, J.A. Swift, *Surface characterization of cholesterol monohydrate single crystals by chemical force microscopy*, Langmuir 18 (12) (2002) 4847–4853.

[79] L.B. Gower, *Biomimetic model systems for investigating the amorphous precursor pathway and its role in biomineralization*, Chem. Rev. 108 (11) (2008) 4551–4627.

[80] N. Unwin, *Structure of a cholinergic cell membrane*, Proc. Natl. Acad. Sci. 119 (34) (2022) e2207641119.

[81] R.S. Abendan, J.A. Swift, *Cholesterol monohydrate dissolution in the presence of bile acid salts*, Cryst. Growth Des. 13 (8) (2013) 3596–3602.

[82] S.M. Ghodsi, et al., *Assessment of pressure and density of confined water in graphene liquid cells*, Adv. Mater. Interfaces 7 (12) (2020) 1901727.

[83] K.S. Dae, et al., *Real-time observation of $CaCO_3$ mineralization in highly supersaturated graphene liquid cells*, ACS Omega 5 (24) (2020) 14619–14624.

[84] M.F. Crook, et al., *EELs studies of cerium electrolyte reveal substantial solute concentration effects in graphene liquid cells*, J. Am. Chem. Soc. 145 (12) (2023) 6648–6657.